na re

ARTICLES

PUBLISHED ONLINE: 27 NOVEMBER 2017 | DOI: 10.1038/NMAT5032

Chiral liquid crystal colloids

Ye Yuan[1†], Angel Martinez[1†], Bohdan Senyuk[1], Mykola Tasinkevych[2,3,4] and Ivan I. Smalyukh[1,5,6*]

Colloidal particles disturb the alignment of rmolecules into a non-chiral liquid crystal (LC) is that they induce chirality of the ensuing mes8–18

benefit from the framework of multipole expansions,[19] which has been extended to nematic colloids[8 18]. Although geometric shape and genus of particles[20 24] allow for controlling elastic multipoles and guiding self-assembly, the role of chirality of colloidal inclusions in controlling these interactions remains unknown.

Here we develop chiral colloidal particles in the forms of left- and right-handed springs and helices suspended in a nematic LC. Using a combination of experiments and computer simulations based on the minimization of Landau de Gennes free energy, we uncover how individual colloidal objects with well-defined chirality impart the symmetry breaking to the nematic host and how the ensuing distortions in the molecular alignment mediate chirality-dependent, elastic colloidal interactions. We explore pair interactions between like- and opposite-handed particles with di erent geometric parameters, revealing unique chirality-controlled e ects, which guide colloidal self-assembly. In nematic hosts with a uniform

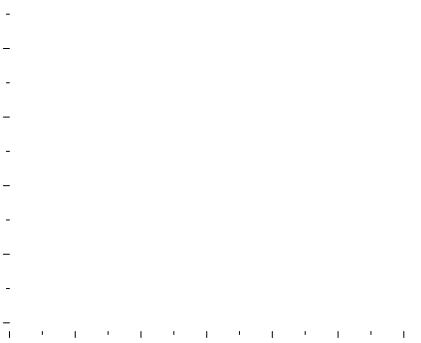

Figure 1 | Microsprings in a nematic liquid crystal. **a**,**b**, Right- and left-handed colloidal springs, respectively, imaged with the help of 3PEF-PM while surrounded by an isotropic medium (immersion oil). **c**,**d**, Self-diffusion of the particles oriented with the spring axis roughly parallel (**c**) or perpendicular (**d**) to n_0. The insets show optical bright-field micrographs at the corresponding orientations with respect to $\mathbf{n}_0$. Solid lines are Gaussian fits to experimental data allowing one to calculate diffusion coefficients[12] along and normal to n_0 (D_k D 2.9 10 ^{3} μm^2 s ^{1}, $D_?$ D 0.93 10 ^{3} μm^2 s ^{1} in **c** and D_k D 3.0 10 ^{3} μm^2 s ^{1}, $D_?$ D 2.7 10 ^{3} μm^2 s ^{1} in **d**). **e**–**j**, Optical micrographs of right- (**e**–**g**) and left-handed (**h**–**j**) colloidal microsprings in 5CB imaged using bright-field (**e**,**h**) and polarizing microscopy without (**f**,**i**) and with (**g**,**j**) an additional phase retardation plate (with the slow axis marked by the yellow double arrow) inserted between the crossed polarizers (white double arrows). **k**–**n**, Detailed analysis of **n**(**r**)-distortions induced in the LC by colloidal springs probed for the same particle using polarizing microscopy (**k**) and 3PEF-PM (**l**–**n**), with **l** and **n** showing details of two individual in-plane 3PEF-PM optical slices obtained for two different linear 3PEF-PM polarizations (marked by the green and red double arrows, respectively) and **m** showing the corresponding 3D perspective view of the particle reconstructed on the basis of superposition of many such slices. Scale bars are 5 μm.

fluorescence polarizing microscopy (3PEF-PM) images (Fig. 1l n). These experiments are consistent with the results of computational modelling based on the minimization of Landau de Gennes free energy, F_{LdG}, of the LC hosting colloidal inclusions (Fig. 2). The experimental finding that the spring axes are more frequently nearly orthogonal to $\mathbf{n}_0$ (Fig. 1d,k n) is consistent with the lower F_{LdG} of this configuration (Fig. 2a). Moreover, both the modelling and experiments reveal that particles equilibrate at orientations where their helical axes tilt slightly away from $\mathbf{n}_0$ (Figs 1c,e j and 2a,f) or the plane orthogonal to it (Figs 1d,k n and 2a,h), with the tilt angles <10 . A detailed analysis of both experimental and theoretical configurations (Figs

Figure 2 | Chirality-dictated alignment of microsprings in a nematic liquid crystal. **a**, Orientation-dependent free energy cost of particle-induced elastic distortions versus the angle between the spring axis $\hat{\boldsymbol{\theta}}_k$ (see **b**–**e** and Supplementary Fig. 1 for the definition of the orthonormal reference frame attached to the particle) and n_0 for different tilt directions of $\hat{\boldsymbol{\theta}}_k$, and for the right- (circles) and left-handed (squares) particles. Open (solid) symbols correspond to the anticlockwise rotation of $\hat{\boldsymbol{\theta}}_k$ about $\hat{\boldsymbol{\theta}}_3(\hat{\boldsymbol{\theta}}_?)$, as shown in –**e**. The insets depict free energy variations near the stable and metastable orientation states. **f**–**i**, Director structures around right-handed springs (**f**,**h**) at energy-minimizing orientations with D 4 (**f**) (blue solid circles in **a**) and with D 86 (**h**) (blue solid circles in **a**), and left-handed springs (**g**,**i**) with D 0 (**g**) (red open squares in **a**) and with D 90 (**i**) (red open squares in **a**) for the metastable (,**g**) and stable (**h**,**i**) particle orientations. **j**–**m**, Detailed director structures and defects corresponding to a colloidal spring shown in **g**. **n**– , Detailed director structures and defects corresponding to a spring shown in **i**. Director structures are shown with rods depicting local orientations of n(r) both at LC–particle interfaces and in the bulk, as well as with colour-coded patterns of azimuthal orientations of n(r) when projected from particle surfaces to the plane orthogonal to n_0, according to the colour scheme in the insets of **g** and **t**, as viewed from different perspectives.

helical axis of the particle, respectively, with $\hat{\boldsymbol{\theta}}_?$ chosen so that the plane spanned by $\hat{\boldsymbol{\theta}}_k$ and $\hat{\boldsymbol{\theta}}_?$ roughly contains the spring's two end faces. We then define $\hat{\boldsymbol{\theta}}_3$ D $\hat{\boldsymbol{\theta}}_k$ $\hat{\boldsymbol{\theta}}_?$. The dependence of F_{LdG} on the tilting directions is well pronounced, especially for the large- branches (compare open and solid symbols in Fig. 2a). When $\hat{\boldsymbol{\theta}}_k$ rotates about $\hat{\boldsymbol{\theta}}_3$ (Fig. 2b,c), the end faces remain roughly parallel to $\mathbf{n}_0$ for all , and in this case numerical calculations predict (almost) identical F_{LdG}( ) for particles of right or left handedness (open symbols in Fig. 2a). However, when $\hat{\boldsymbol{\theta}}_k$ tilts about $\hat{\boldsymbol{\theta}}_?$ (Fig. 2d,e), the end faces form an angle of approximately with $\mathbf{n}_0$. Since the faces

© 2017 Macmillan Publishers Limited, part of Springer Nature. All rights reserved.

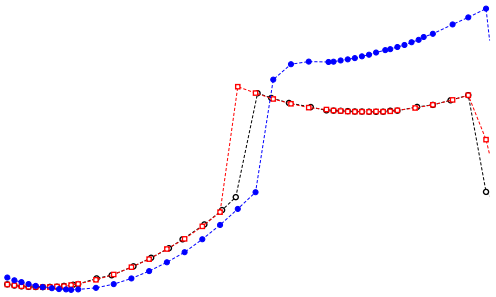

Figure 3 | Chirality-dictated alignment of single helices in a nematic liquid crystal. **a**–**f**, Optical micrographs of left-handed microhelices obtained using bright-field (**a**,**d**) and polarizing microscopy without (**b**,**e**) and with (**c**,**f**) a phase retardation plate. **g**,**h**, Self-diffusion of particles oriented with θ_k roughly orthogonal (**g**) and parallel (**h**) to n_0. The insets show optical bright-field micrographs at the corresponding orientations with respect to n_0 (D_k $D_?$ 2.2 10 ^{3} μm^2 s ^{1} in **g** and D_k 2.7 10 ^{3} μm^2 s ^{1}, $D_?$ 0.68 10 ^{3} μm^2 s ^{1} in **h**). **i**, Orientation-dependent free energy cost of elastic distortions induced by particles versus the angle between θ_k and n_0 for different orientations of the tilt direction of θ_k, for left- (squares) and right-handed (circles) helices. Open (solid) symbols correspond to anticlockwise rotation of θ_k about θ_3($\theta_?$), as shown in Fig. 2b–e. The insets depict free energy variations near the stable and metastable orientation states. **j**–**m**, Director structures around right-handed helices at D8 (**j**) (blue solid circles in **i**) and at D82 (**l**) (blue solid circles in **i**) and left-handed helices at D0 (**k**) (red open squares in **i**) and at D90 (**m**) (red open squares in **i**), which are stable (**j**,**k**) and metastable (**l**,**m**) particle orientations. The director field is shown with the help of rods and colour-coded azimuthal orientations of n(r) on particle surfaces relative to n_0 according to the colour scheme shown in the inset of **k**. Scale bars are 5 μm.

impose tangential anchoring on **n**(**r**), their misalignment with $\mathbf{n}_0$ is penalized by additional elastic free energy costs, yielding the *F*

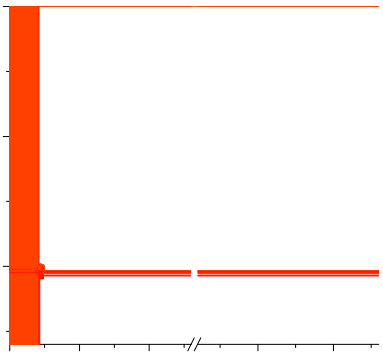

Figure 4 | Chirality-dependent pair interactions of colloidal springs. **a**, Time-colour-coded trajectory of attraction of like-handed microsprings initially separated along n_0. The bottom inset shows colour scale of elapsed time counted from the moment of releasing particles from laser traps (t_{min}) until the moment when they approach each other at t_{max} (t_{max} t_{min} D 27 s), as shown in the bright-field micrographs in the inset. The final self-assembled colloidal structure for the same particles at t D 35 s > t_{max} is also shown in the inset in a slightly enlarged micrograph and emerges as a result of additional rotation of the colloidal springs around their axes. **b**, Separation distance d versus time corresponding to **a**, with the distance dependence of the corresponding interaction force shown in the inset. **c**, Time-colour-coded trajectory of repulsion of like-handed microsprings initially separated so that the separation vector is orthogonal to n_0. **d**, Time-colour-coded trajectory of repulsion of opposite-handed microsprings initially separated along n_0. The insets show the corresponding optical micrographs of the interacting particles. **e**, Separation distance versus time corresponding to **d**; the distance dependence of the corresponding interaction force is shown in the inset. **f**, Time-coded trajectory of attraction of opposite-handed microsprings initially separated so that the separation vector is orthogonal to n_0. The red curves in **b**,**e**, are the best fits of the experimental data with $d(t)$ D $(d_0^n$ n $t)^{1=n}$ where n D 5 for dipole–dipole interaction[21]; the fitting coe□cients are d_0 D 25 μm, D 1.3 10^5 μm^5 s ^{1} in **b** and d_0 D 29 μm, D 0.46 10^5 μm^5 s ^{1} in **e**. Solid red lines in the insets of **b** and **e** are the best linear fits with[21] ln F D (n 1) ln d C const. Scale bars are 5 μm.

are consistent with what is expected for chiral elastic dipoles recently introduced within the approach of nematostatics[17], where left- and right-handed springs have opposite orientations of the dipole moments. Numerical modelling reproduces details of the experimentally observed colloidal behaviour (Fig. 5 and Supplementary Fig. 5), providing additional insights into the physical underpinnings. Thus, in Fig. 5a,b we plot F_{LdG} as a function of the angle between **d** and $\mathbf{n}_0$ for like- and opposite-handed springs, respectively, and at a fixed centre-to-centre distance d. The particles' $\hat{\boldsymbol{\theta}}_k$ axes are aligned along $\mathbf{n}_0$ and di erent curves correspond to di erent orientations of **d** relative to particle frames. In agreement with the experiments and nematostatics[17], the like-handed pair of particles tends to align **d** along $\mathbf{n}_0$ with F_{LdG}( ) having minima at 0 and 180 (Fig. 5a), while the opposite-handed ones align **d** orthogonal to $\mathbf{n}_0$, with F_{LdG}( ) minimized at 90 (Fig. 5b). The behaviour of the free energy versus d at D 0 , depicted in Fig. 5c,d for pair interactions of like- and opposite-handed springs, respectively, also agrees with the experiments and nematostatics: the like-handed springs attract (Fig. 5c) while opposite-handed ones repel (Fig. 5d) along $\mathbf{n}_0$. At relatively large inter-particle distances (see experimental data in Fig. 4b,e and numerically computed dependencies in Fig. 5c,d), colloidal interaction potentials and forces scale with distance as $/ d^{-3}$ and $/ d^{-4}$, respectively, consistent with the dipolar nature of interactions. At small distances, the departures from these power-law dependencies are caused by the influence of the higher-order elastic multipoles and nonlinear near-field e ects that cannot be captured within the multipole expansion analysis, but are revealed by numerical modelling. For example, F_{LdG} exhibits a local minimum at small distances (Fig. 5d), which is related to boojum sharing between proximal end faces.

Both experimental and computational studies of pair interactions reveal the well-defined role of chirality in controlling colloidal elastic pair interactions, which can be generalized to other chiral colloids in LCs and used in conjunction with particle shape to predefine self-assembly. To provide an example of how the interplay of shape and chirality can further enrich colloidal behaviour, we probe pair interactions between colloidal helices (Supplementary Fig. 6) and elucidate many subtle e ects. The colloidal helices are found to attract starting from initial conditions with all possible orientations of **d** relative to $\mathbf{n}_0$ and for both like- and opposite-handed

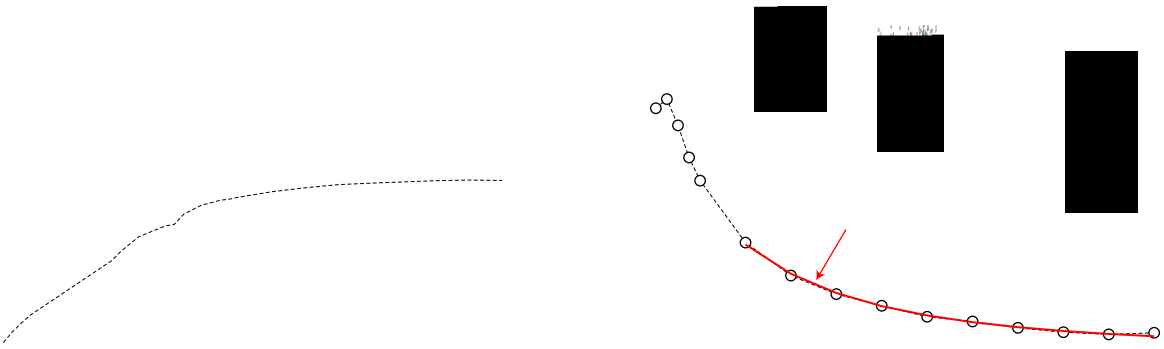

Figure 5

Figure 6 | Twisting of chiral particles relative to each other. **a**, Numerically calculated Landau–de Gennes free energy as a function of the angle $_?$ between the axes of like-handed springs, for the case when these spring axes rotate about the particles' $\hat{\theta}_?$ vectors in opposite directions and by equal amounts, as is shown schematically in **e**. The spring centre-to-centre vector **d** is fixed with d D 1.625R and with the angle between **d** and $\mathbf{n}_0$ at 90 . **b**, Free energy as a function of d at $_?$ D 180 , all the other parameters are the same as in **a**. The insets in **a**,**b** show the director configurations around the springs with the help of rods and colour-coded azimuthal orientations, with respect to $\mathbf{n}_0$, of $\mathbf{n}(\mathbf{r})$ on particle surfaces. **c**,**d**, The case of like- (circles) and opposite-handed (squares) springs, depicting the free energy variations with $_?$ (particles' axes rotate about $\hat{\theta}_?$) or $_k$ (particles' axes rotate about $\hat{\theta}_3$) at d D 1.625R and D 90 , near the stable (**d**) and metastable (**c**) orientation states. Open (solid) symbols correspond to the case when the spring axes $\hat{\theta}_k$ rotate about particles' aligned $\hat{\theta}_?$ vectors, see **e** ($\hat{\theta}_3$ vectors, see **f**) in opposite directions by equal amounts.

which lead to the mutual alignment of non-chiral dipole moments orthogonal to $\mathbf{n}_0$ of two chiral helices so that the interactions are attractive. Computational modelling of nematic colloids with di er-ent geometry (Supplementary Figs 7 9) supports this observation and provides additional insights into this behaviour. Supplementary Fig. 7 presents the free energy cost F_{LdG} of elastic distortions at fixed

between the $\hat{\boldsymbol{\theta}}_k$ axes has a local minimum at $_{?}$ 16 (open circles in Fig. 6c) and a global minimum at $_{?}$ 176 (open circles in Fig. 6d), indicating the intrinsic tendency of springs to twist when they are placed side-by-side, with $\mathbf{d}$? $\mathbf{n}_0$. Supplementary Fig. 8a illustrates the twisting tendency of like-handed helices: $F_{LdG}(\ _{?})$ shows only a global minimum at $_{?}$ D 12 . Contrary to the case of the springs, this configuration for helices is stable relative to the variation of d (Supplementary Fig. 8c), resulting in helicoidal assemblies of particles. Opposite-handed springs aligned along $\mathbf{n}_0$ also exhibit the twisting tendency when placed side-by-side (see the data presented by squares in Fig. 6c,d). However, the twisting direction is sensitive to the placement of springs relative to each other (compare the open and the solid squares in Fig. 6c,d and Supplementary Fig. 9a). Racemic dispersions of left- and right-handed chiral particles do not possess helicoidal ordering (Fig. 5g,h), showing that opposite-handed chiral particles cannot form chiral superstructures.

Conclusions

We have demonstrated that chirality of colloidal particles interplays with the nematic elasticity to predefine chiral or racemic superstructures. Chirality induced by dilute colloidal dispersions competes with the boundary conditions on confining surfaces to yield unwound configurations in which 80 loC-7(hic)-361per3(s)3-10(3(.)DM84-10.46100044Tdr)13(der)-6(in)8(g)]TJ0faesd

Methods